Channelization cascade in landscape evolution

Landscape channelization cascade

Sara Bonetti[a], **Milad Hooshyar**[b,c], **Carlo Camporeale**[d], **and Amilcare Porporato**[b,c,1]

[a]Department of Environmental Systems Science, ETH Zurich, 8092 Zurich, Switzerland; [b]Department of Civil and Environmental Engineering, Princeton University, Princeton, New Jersey 08544, USA; [c]Princeton Environmental Institute, Princeton university, Princeton, New Jersey 08544, USA; [d]Department of Environment, Land and Infrastructure Engineering, Politecnico di Torino, 10129 Turin, Italy

This manuscript was compiled on December 1, 2019

The hierarchy of channel networks in landscapes displays features that are characteristic of non-equilibrium complex systems. Here we show that a sequence of increasingly complex ridge and valley networks is produced by a system of partial differential equations coupling landscape evolution dynamics with a specific catchment area equation. By means of a linear stability analysis we identify the critical conditions triggering channel formation and the emergence of characteristic valley spacing. The ensuing channelization cascade, described by a dimensionless number accounting for diffusive soil creep, runoff erosion, and tectonic uplift, is reminiscent of the subsequent instabilities in fluid turbulence, while the structure of the simulated patterns is indicative of a tendency to evolve toward optimal configurations, with anomalies similar to dislocation defects observed in pattern-forming systems. The choice of specific geomorphic transport laws and boundary conditions strongly influences the channelization cascade, underlying the nonlocal and nonlinear character of its dynamics.

Ridge and valley patterns | Landscape evolution model | Detachment limited | River networks | Drainage area

The spatial distribution of ridges and valleys, including the formation of evenly spaced first order valleys as well as more complex branching river networks (see Fig. 1), is one of the most striking features of a landscape. It has long fascinated the scientific community, leading to the development of a rich body of work on the statistical, theoretical, and numerical analysis of landscape organization. Early works focused on the definition of stream ordering systems for the river basin characterization (1–3) and the coupled dynamics of water and sediment transport to identify stability conditions for incipient valley formation (4–6), followed by the statistical description of river networks, including scaling laws and fractal properties of river basins (7–10), the related optimality principles (9, 11), and stochastic models (12–14). These studies have shed light on the spatial organization and governing statistical laws of developed river networks and explored the linkages to other branch-forming systems (13, 15, 16), but have not tackled the physical origin of the underlying instabilities and feedback mechanisms acting over time in the formation of the observed ridge and valley patterns (17). To this purpose, landscape evolution models have been employed for the analysis of branching river networks (18, 19) in relation to the main erosional mechanisms acting on the topography. These works represented an important step forward in the study of spatially organized patterns of ridges and valleys. However, lacking a rigorous formulation of the drainage area equation (20, 21) precluded the theoretical investigation of the underlying instabilities in relation to the leading geomorphological processes involved.

In this work, we focus on landscapes characterized by runoff erosion, expressed as a function of the specific drainage area a (21) to obtain grid-independent solutions without the introduction of additional system parameters. The resulting system of coupled, nonlinear partial differential equations (PDEs) provides a starting point for the theoretical analysis of channel-forming instabilities and landscape self-organization and allows us to describe the resulting ridge and valley patterns as a function of the relative proportions of diffusive soil

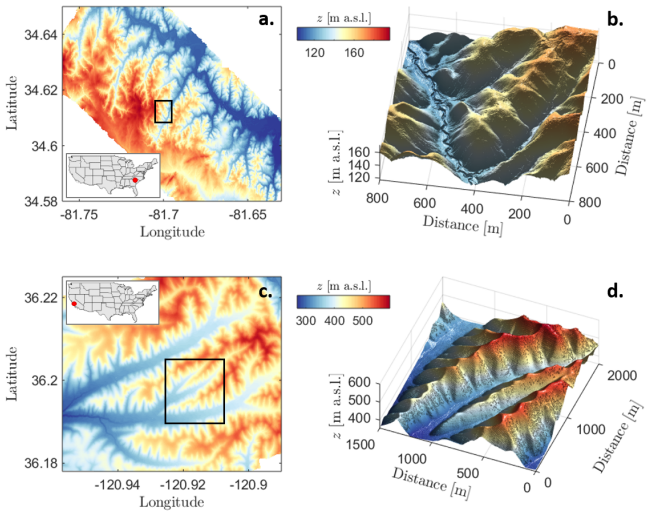

Fig. 1. Ridge and valley patters in natural landscapes. 1-meter resolution LiDAR topographies of (a) the Calhoun Critical Zone landscape in South Carolina and (b) Gabilan Mesa in California. Panels b and d show three-dimensional surfaces for two subsets (black rectangles in panels a and c) where regular evenly spaced valleys are visible. Data were obtained from the National Center for Airborne Laser Mapping (NCALM) and retrieved from the OpenTopography facility.

Significance Statement

We show that a sequence of increasingly complex ridge and valley networks is produced by a system of nonlinear partial differential equations serving as a minimalist landscape evolution model describing the interplay between soil creep, runoff erosion, and tectonic uplift. We identify the critical conditions for the transition from a smooth to a channelized topography by means of a linear stability analysis and highlight striking similarities with fluid dynamic turbulence. The results shed light on the physical mechanisms responsible for observed landscape self-organization. The formation of regular pre-fractal networks reveals the tendency of the system to evolve towards optimal configurations typical of non-equilibrium complex systems.

Author contributions: S.B. and A.P. designed research, discussed results, and wrote the paper. S.B. and M.H. performed the numerical simulations, while S.B., C.C., and A.P. performed the linear stability analysis. All the authors reviewed and edited the final version of the manuscript.

The authors declare no conflict of interest.

[1]To whom correspondence should be addressed. E-mail: aporpora@princeton.edu

creep, runoff erosion, and tectonic uplift. The nonlocal character of the equations makes the boundary conditions extremely important. On regular (i.e., square and rectangular) domains, simulations reveal a sequence of channel instabilities reminiscent of the laminar-to-turbulent transition (22–24). The explicit mathematical structure makes it possible to perform a linear stability analysis of the coupled PDE system to identify the critical conditions for the first channel-forming instability. The subsequent branching sequence towards smaller and smaller valleys until soil creep becomes dominant is similar to the turbulent cascade with large scale vortices leading to smaller ones until viscous dissipation. The formation of networks of ridges and valleys, brought about by the regular boundary conditions, also reveals the tendency of the system to develop configurations suggestive of optimization principles (11) typical of non-equilibrium thermodynamics and complex systems (16, 25–32). Our analysis is different from recent interesting contributions on groundwater-dominated landscapes (33, 34), where branching and valley evolution is initiated at seepage points in the landscape.

Landscape evolution in detachment-limited conditions

The time evolution of the surface elevation $z(x, y, t)$ is described by the sediment continuity equation (17, 18, 35, 36)

$$\frac{\partial z}{\partial t} = U - \nabla \cdot \mathbf{f} = U - \nabla \cdot (\mathbf{f_d} + \mathbf{f_c}), \qquad [1]$$

where t is time, U is the uplift rate, and $\mathbf{f}$ is the total volumetric sediment flux, given by the sum of fluxes related to runoff erosion/channelized flow ($\mathbf{f_c}$) and soil creep processes ($\mathbf{f_d}$). The soil creep flux is assumed to be proportional to the topographic gradient (37, 38), hence $\mathbf{f_d} = -D\nabla z$, D being a diffusion coefficient (here assumed to be constant in space and time). In the so-called detachment-limited (DL) conditions (6, 18, 39) it is assumed that all eroded material is transported outside the model domain, so that no sediment redeposition occurs. Under these conditions, the runoff erosion term is approximated as a sink term given by (18) $\nabla \cdot \mathbf{f_c} \approx K'_a |\nabla z|^n q^m$, where K'_a is a coefficient, q is the discharge per unit width of contour line, and m and n are model parameters. As a result, Eq. (1) becomes

$$\frac{\partial z}{\partial t} = D\nabla^2 z - K'_a q^m |\nabla z|^n + U. \qquad [2]$$

Thus the soil creep flux results in a diffusion term which tends to smooth the surface, while the runoff erosion component is a sink term which excavates the topography as a function of local slope and specific water flux.

The surface water flux q is linked to the continuity equation

$$\frac{\partial h}{\partial t} = R - \nabla \cdot (q\mathbf{n}) \qquad [3]$$

where h is the water height, $\mathbf{n}$ the direction of the flow, and R the rainfall rate effectively contributing to runoff production. Eq. (3) can be simplified assuming steady-state conditions with constant, representative rainfall rate, R_0, and (as in previous works (40)) constant speed of water flow v_0 in the direction opposite to the landscape gradient (i.e., $\mathbf{n} = -\nabla z/|\nabla z|$). In such conditions, it can be shown (21) that the water height, h, and the specific water flux, q, are both proportional to the specific contributing area, a, i.e. $h = q/v_0 = aR_0/v_0$. As a result, the system of Eqs. (3) - (2) reduces to an equation for the specific catchment area a (21),

$$-\nabla \cdot \left(a \frac{\nabla z}{|\nabla z|} \right) = 1, \qquad [4]$$

coupled to the landscape evolution equation

$$\frac{\partial z}{\partial t} = D\nabla^2 z - K_a a^m |\nabla z|^n + U, \qquad [5]$$

with an adjusted erosion constant K_a to account for the proportionality between a and q.

It is important to observe that the specific drainage area a has units of length and is related to the drainage area A as $a = \lim_{w\to 0} A/w$; it is thus defined per unit width of contour line w (21). Most landscape evolution models (e.g., 9, 18, 41, 42) use the total drainage area A in Eq. (5) instead of a, with several notable implications. The value of A is generally evaluated using numerical flow-routing algorithms (e.g., D8, D∞ (43)) which provide grid-dependent values of A. To correct for this, the drainage area A is often modified to account for the channel width (18, 41), but this results in approximations with arbitrary parameters. Conversely, the use of a avoids grid-dependence of the resulting topography. Moreover, re-casting the problem in terms of a consistent coupled system of PDEs makes it possible to analyze theoretically the landscape evolution process. As detailed below (see Methods), an analytic solution for the steady state hillslope profile can be derived (44) and then used as a basic state for a linear stability analysis to identify the critical conditions for the first channel formation and the characteristic valley spacing.

It is useful to non-dimensionalize the system of Eqs. (4) and (5) to quantify the relative impact of soil creep, runoff erosion, and uplift on the landscape morphology. Using a typical length scale of the domain, l, and the parameters of Eqs. (4) and (5), the following dimensionless quantities can be introduced: $\hat{t} = \frac{tD}{l^2}$, $\hat{x} = \frac{x}{l}$, $\hat{y} = \frac{y}{l}$, $\hat{z} = \frac{zD}{Ul^2}$, and $\hat{a} = \frac{a}{l}$. With these quantities, Eq. (5) becomes

$$\frac{\partial \hat{z}}{\partial \hat{t}} = \hat{\nabla}^2 \hat{z} - \mathcal{C}_\mathcal{I} \hat{a}^m |\hat{\nabla} \hat{z}|^n + 1 \qquad [6]$$

where

$$\mathcal{C}_\mathcal{I} = \frac{K_a l^{m+n}}{D^n U^{1-n}}. \qquad [7]$$

As we will see later, this index describes the tendency to form channels in a way which is reminiscent of the global Reynolds number (defined as the ratio of inertial to viscous forces) in fluid mechanics, as well as of the ratio of flow permeabilities used in constructal theory (45). A similar quantity based on a local length scale (i.e., the mean elevation of the emerging topographic profile) was used in Perron et al. (18). The definition of $\mathcal{C}_\mathcal{I}$ as a function of global variables based on system parameters (e.g., uplift rate U) and boundary conditions allows us to directly infer system behavior. For example, when the slope exponent n is equal to 1, the relative proportion of runoff erosion and soil creep can be seen to be independent of the uplift rate; however, if $n > 1$ the uplift acts to increase the runoff erosion component, while for $n < 1$ it enhances the diffusive component of the system. As we will see, this results in different drainage-network patterns as a function of uplift rates.

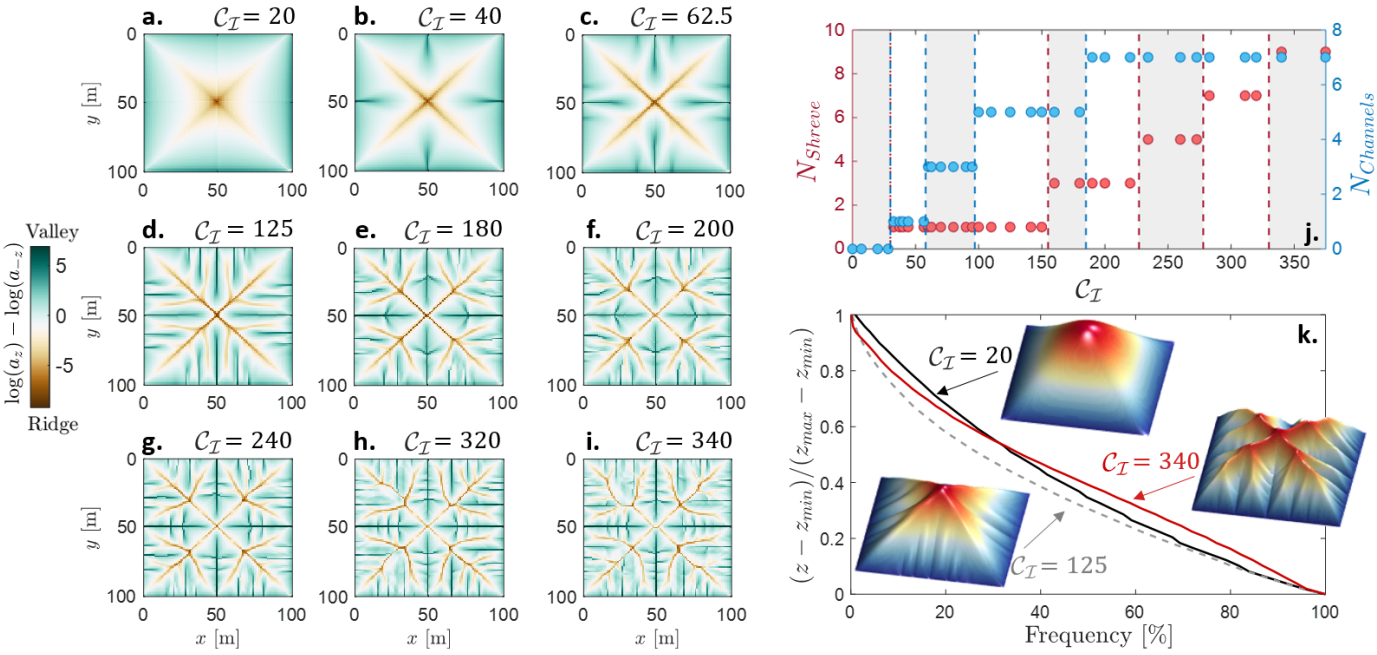

Fig. 2. Channelization cascade. Simulation results obtained for $m = 0.5$ and $n = 1$. (a-i) Ridge and valley patterns obtained for $\mathcal{C}_\mathcal{I}$ values equal to 20, 40, 62.5, 125, 180, 200, 240, 320, and 340: brown corresponds to ridges and green to valleys. To better highlight the ridge and valley structure we show here the difference between the specific drainage area a and the specific dispersal area a_{-z} (i.e., the value of a computed over the flipped topography - see ref. 20). (j) Highest Shreve order (red) and number of main channels on each domain side (blue) for different values of the dimensionless parameter $\mathcal{C}_\mathcal{I}$. Based on the number of channels and the Shreve order nine regimes can be identified with distinctively different ridge/valley patterns (shown in panels a-i). (k) Normalized hypsometric curves obtained for $\mathcal{C}_\mathcal{I}$ = 20 (solid black), 125 (dashed gray), and 340 (solid red): when no secondary branching is observed (i.e., $\mathcal{C}_\mathcal{I} \lesssim 155$) the hypsometric curve is concave, while after the first secondary branching is formed it undergoes a transition to a shape concave for higher elevations and convex at low elevations. Insets in panel k show 3d plots of the steady state topographies for the three cases, the color code represents surface elevation (red = high, blue = low).

Results

Organized ridge and valley patterns. Simulation results obtained by numerically solving Eqs. (4)-(5) over square domains with $m = 0.5$ and $n = 1$ (see Methods for details) are shown in Fig. 2. The emerging ridge/valley patterns are classified in terms of Shreve order (used here as a measure of branching complexity - see ref. 3), and number of channels formed on each side of the domain. As can be seen from Eq. (7), for $n = 1$ the dimensionless parameter $\mathcal{C}_\mathcal{I}$ is independent of the uplift rate, so that the spatial patterns of Fig. 2 are only a function of the relative proportions of the soil creep and runoff erosion components. For low $\mathcal{C}_\mathcal{I}$ values (i.e., $\lesssim 30$) no channels are formed and the topography evolves to a smooth surface dominated by diffusive soil creep (Fig. 2a). As the runoff erosion coefficient is increased the system progressively develops one, three, and five channels on each side of the square domain for $30 \lesssim \mathcal{C}_\mathcal{I} \lesssim 58$, $58 \lesssim \mathcal{C}_\mathcal{I} \lesssim 97$, and $97 \lesssim \mathcal{C}_\mathcal{I} \lesssim 155$, respectively (Fig. 2b-d). When $\mathcal{C}_\mathcal{I}$ is increased above ≈ 155 the central channels develop secondary branches, with the main central channel becoming of Shreve order three (Fig. 2e). As $\mathcal{C}_\mathcal{I}$ is further increased seven channels can be observed originating on each side of the domain, and the main central channel further branches (Fig. 2f-i) becoming of order nine for the highest $\mathcal{C}_\mathcal{I}$ used for this configuration.

As the resulting landscape changes from a smooth topography to a progressively more dissected one, the shape of the hypsometric curve varies from concave (i.e., slope decreases along the horizontal axis) to one with a convex portion for low elevations (Fig. 2k). In particular, channel formation (with no secondary branching) causes the hypsometric curve to progressively lower as a result of the lower altitudes observed in the topography, while maintaining a concave profile. As secondary branches develop, the hypsometric curve shifts to a concave/convex one, with the convex portion at lower altitudes becoming more evident as $\mathcal{C}_\mathcal{I}$ increases (see red line for $\mathcal{C}_\mathcal{I} = 340$ in Fig. 2k).

The striking regularity of the drainage and ridge patterns induced by the simple geometry of the domain is reminiscent of regular pre-fractal structures (e.g., Peano basin (8, 9, 46–48)) and is indicative of the fundamental role of boundary conditions due to the highly non-local control introduced by the drainage area term. The introduction of noise and irregular boundaries quickly breaks the regularity of the patterns (see results from numerical simulations obtained over progressively more irregular boundaries in the SI Appendix, Fig. S10). The ridge and valley networks of Fig. 2 highly resemble Fig. 5 in ref. 31, where optimized tree-shaped flow paths were constructed to connect one point to many points uniformly distributed over an area. We further highlight similarities with the patterns obtained in ref. 30 by means of an erosion model where the global flow resistance is minimized.

Effect of runoff erosion laws. The effect of different runoff erosion laws has been discussed in the literature (42) also in relation to climate, vegetation cover, and soil properties (49, 50). Their role was analyzed here by changing the values of the exponents n and m, as shown in Fig. 3.

When the value of n is different from unity, the resulting ridge/valley patterns depend on the uplift rate U, as per Eq. (7). When n is increased the system displays channelization and secondary branching for higher values of $\mathcal{C}_\mathcal{I}$ (i.e.,

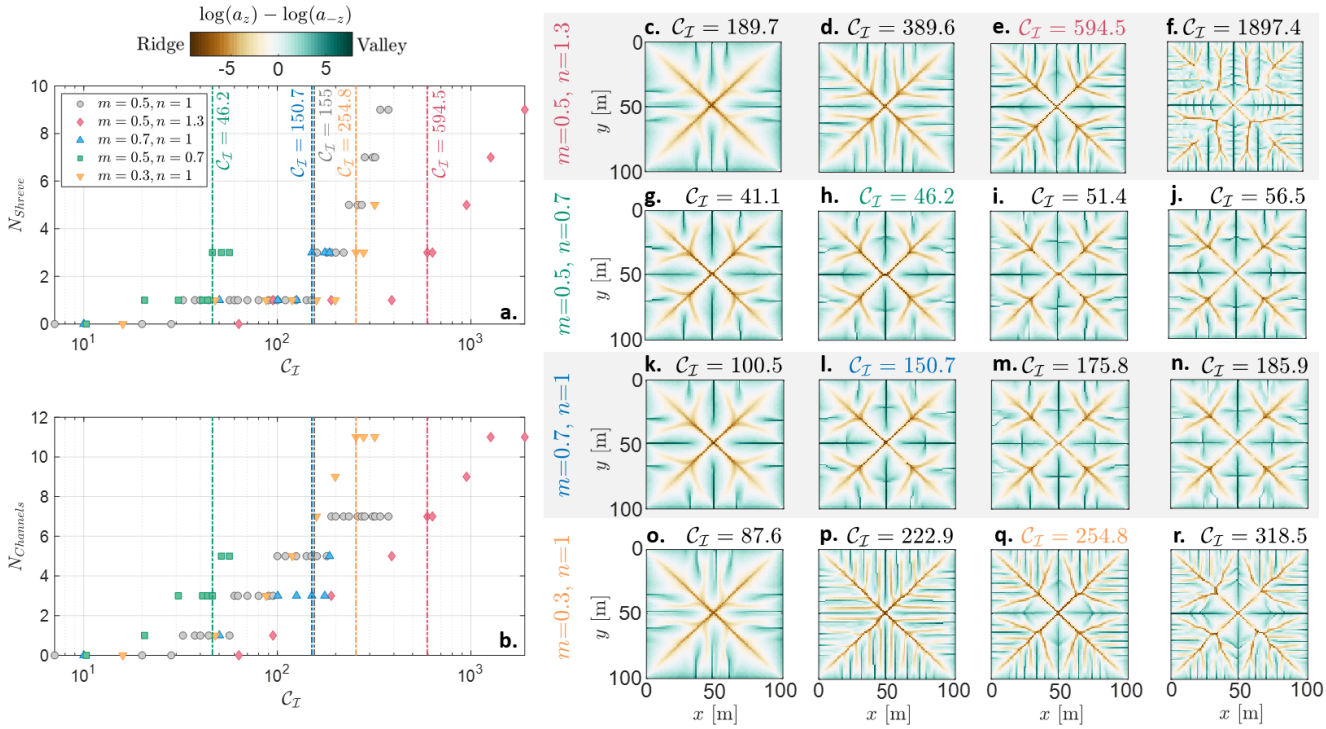

Fig. 3. Effect of runoff erosion laws. Simulation results obtained for different values of the slope and runoff exponents (i.e., n and m): (a) maximum Shreve order and (b) number of channels on each domain side as a function of $\mathcal{C}_\mathcal{I}$. Colored dash-dotted lines mark the $\mathcal{C}_\mathcal{I}$ values at which the first secondary branching is observed for each set of m and n values, and the corresponding ridge/valley patterns are highlighted in panels c-r. (c-r) Examples of two-dimensional ridge (brown) and valley (green) patterns for scenarios with (c-f) increased slope exponent ($n = 1.3$, $m = 0.5$, and $\mathcal{C}_\mathcal{I} = 189.7$, 389.6, 594.5, 1897.4), (g-j) decreased slope exponent ($n = 0.7$, $m = 0.5$, and $\mathcal{C}_\mathcal{I} = 41.1$, 46.2, 51.4, 56.6), (k-n) increased water flux exponent ($n = 1$, $m = 0.7$, and $\mathcal{C}_\mathcal{I} = 100.5$, 150.7, 175.8, 185.9), and (o-r) decreased water flux exponent ($n = 1$, $m = 0.3$, and $\mathcal{C}_\mathcal{I} = 87.6$, 222.9, 254.8, 318.5).

points are shifted to the right in Fig. 3a,b), with a more dissected planar geometry characterized by narrower valleys and smaller junction angles (Fig. 3c-f). A decrease in n leads to smoother geometries with wider valleys and the first secondary branching developing when only three channels per each side of the domain are present (see Fig. 3g-j). This results in a hypsometric curve with a more pronounced basal (i.e., at low altitudes) convexity for $n > 1$, as a consequence of the progressively more dissected topography (see SI Appendix, Fig. S2).

As m is increases (Fig. 3k-n) the system develops secondary branching when only three channels are present on each side of the domain, with the formation of less numerous but wider valleys with higher junction angles, and a reduced basal convexity in the hypsometric curve (see SI Appendix, Fig. S2). Conversely, a decrease in m results in a more dissected landscape, with narrower valleys (Fig. 3o-r) and a more pronounced transition of the hypsometric curve to a convex shape for low altitudes (see SI Appendix, Fig. S2).

Wide rectangular domains. To assess boundary-condition effects on branching patterns we also considered very wide rectangular domains ($\mathcal{C}_\mathcal{I}$ is constructed using the distance between the longest sides). Besides numerical investigation, in this case an analytical solution is possible for the unchannelized case (for $m = 1$ and $n = 1$, see Methods), around which we also performed a linear stability analysis. In our analogy with turbulent flows, the case of wide rectangular domains corresponds to the flow of viscous fluids between parallel plates (23, 24).

Results from the linear stability analysis are shown in Fig. 4. A critical value $\mathcal{C}_{\mathcal{I},c} \approx 37$ for the first channel instability is identified, corresponding to a characteristic valley spacing λ_c of approximately 42 m, in line with observations (an analysis of five landscapes in the continental US from ref. 51 provides values of valley spacing ranging between approximately 30 and 300 m). As $\mathcal{C}_\mathcal{I}$ further increases (i.e., runoff erosion increases with respect to diffusion) the predicted valley spacing is reduced (see Fig. 4c), with the formation of progressively narrower valleys. Results from the linear stability analysis are in line with predictions from numerical experiments conducted over large rectangular domains, where the first channel instability occurs at $\mathcal{C}_{\mathcal{I},c} \approx 32$ with a valley spacing $\lambda_c \approx 33$ m. Analogously to the Orr-Sommerfeld problem for plane Poiseuille flow, the system here presents a Type I linear instability (52). Insight on the role of the m and n exponents on the critical channelization index $\mathcal{C}_{\mathcal{I},c}$ and related valley spacing was obtained from numerical experiments. As shown in the SI Appendix (Fig. S9), as the water flow exponent m decreases, the value of $\mathcal{C}_\mathcal{I}$ at which the first channel forming instability occurs increases and the valley spacing decreases. This is in agreement with results obtained over square domains (Fig. 3) where a decrease in the value of m resulted in a more dissected landscape with narrower valleys.

The numerical simulations confirm the results of the linear stability analysis and are in agreement with those of ref. 18. Fig. 5 compares the drainage patterns obtained as a function of $\mathcal{C}_\mathcal{I}$ for rectangular domains of size 100 m by 500 m. As for the square domain, for small $\mathcal{C}_\mathcal{I}$ values the soil creep component dominates resulting in an unchannelized smooth topography

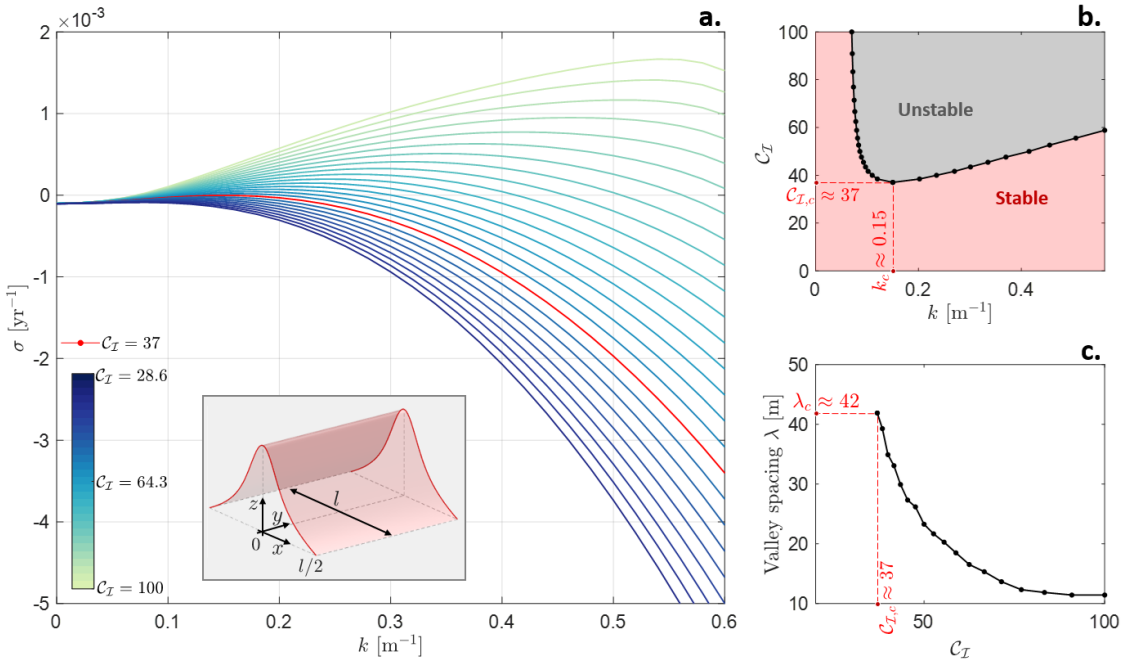

Fig. 4. Linear stability analysis. (a) Growth rate σ as a function of wavenumber k for different values of the dimensionless number $\mathcal{C}_\mathcal{I}$, (b) marginal stability curve (the solid line marks the instability of the basic state to channel initiation), and (c) characteristic valley spacing λ as a function of the dimensionless number $\mathcal{C}_\mathcal{I}$. The linear stability analysis predicts a critical value $\mathcal{C}_{\mathcal{I},c} \approx 37$ for the first channel instability (with valley spacing $\lambda_c \approx 42$ m). The inset in panel (a) shows the geometry assumed as a basic state for the linear stability analysis and for the derivation of the theoretical hillslope profiles (see also Methods).

(Fig. 5a). After the first channelization, valleys tend to narrow as $\mathcal{C}_\mathcal{I}$ increases until the first secondary branching occurs (Fig. 5b,c). Further increasing the runoff erosion component provides progressively more dissected landscapes with the emergence of secondary branching (Fig. 5d-f). As in turbulent flows larger Reynolds numbers produce smaller and smaller vortices, here increasing $\mathcal{C}_\mathcal{I}$ leads to finer and finer branching (the resolution of which becomes quickly prohibitive from a computational standpoint).

The mean elevation profiles, computed as average elevation values along the x axis and neglecting the terminal parts of the domain to avoid boundary effects, are shown in Fig. 5g-l. As the topography becomes progressively more dissected with increasing $\mathcal{C}_\mathcal{I}$, the mean elevation profile tends to become more uniform (Fig. 5g-l). Such a behavior of the mean elevation profiles for increasing $\mathcal{C}_\mathcal{I}$ is similar to the flattening of turbulent mean velocity profiles with increasing Reynolds number (24).

The transition from a smooth to a channelized topography with increasing $\mathcal{C}_\mathcal{I}$ is reflected in the behavior of the quantity $DS_*/Ul = f(\mathcal{C}_\mathcal{I}, m)$, which describes the ratio of the outgoing diffusive flux and the incoming uplift sediment flux at the hillslope base, S_* being the slope of the mean elevation profile at the hillslope base (see Methods for details). Fig. 5p shows the relationship between DS_*/Ul and $\mathcal{C}_\mathcal{I}$ obtained from numerical simulations for $n = 1$ and different values of the exponent m. For small $\mathcal{C}_\mathcal{I}$ values the numerical results match the analytic relationship for the smooth surface (Eq. (11)) and deviate from it at $\mathcal{C}_{\mathcal{I},c} \approx 32$ where the first channel-forming instability occurs. Continuing our analogy with turbulence, the behavior of DS_*/Ul as a function of $\mathcal{C}_\mathcal{I}$ closely resembles that of the friction factor with increasing Reynolds number (see Methods as well as figure 7.3 in ref. 53).

The effect of boundary conditions on the spatial regularity of ridge and valley patterns becomes especially apparent when comparing simulations with different aspect ratios. As can be seen in Fig. 5m-o, when the domain size is slightly changed, the spatial organization of ridges and valleys is modified (see, e.g., the more regular pattern obtained for $\beta = 4.6$ compared to $\beta = 5.1$), while the mean elevation profiles remain practically invariant (see SI Appendix, Fig. S8). This suggests that some optimal domain length is needed to accommodate the formation of regular ridge and valley patterns (this is also evident from an analysis of cross-sections along the longer sides of the domain, see Figs. S3-S7 in the SI Appendix). This results in the formation of dislocation defects, as highlighted in the example of Fig. 5m-o, as it is typical in nonlinear pattern-forming PDEs (52).

Discussion and conclusions

A succession of increasingly complex networks of ridges and valleys was produced by a system of nonlinear PDEs serving as a minimalist model for landscape evolution in detachment-limited conditions. The sequence of instabilities is reminiscent of the subsequent bifurcations in fluid dynamic instabilities (23, 24, 52) and is captured by a dimensionless number ($\mathcal{C}_\mathcal{I}$) accounting for the relative importance of runoff erosion, soil creep, and uplift in relation to the typical domain size. Tantalizing analogies with fluid turbulence, and in general with other driven non-equilibrium systems in which a hierarchical pattern develops toward finer scales, can also be observed in the competition between runoff erosion and soil creep (which resembles the competition between viscous and inertial forces), the reduction of the minimum branching scale with $\mathcal{C}_\mathcal{I}$, and the flattening of the mean hypsometric curves as the channelization is increased.

Characteristic spatial configurations were shown to emerge over both square and rectangular domains from the trade-off between diffusion and erosion. The striking regularity of the ridge and valley networks, with the characteristics of regular pre-fractals (e.g., the Peano basin (8, 46–48)), is quickly lost as effects of noise and irregular boundaries are introduced (see SI Appendix, Fig. S10). The shape of the hypsometric curve depends on the level of channelization and

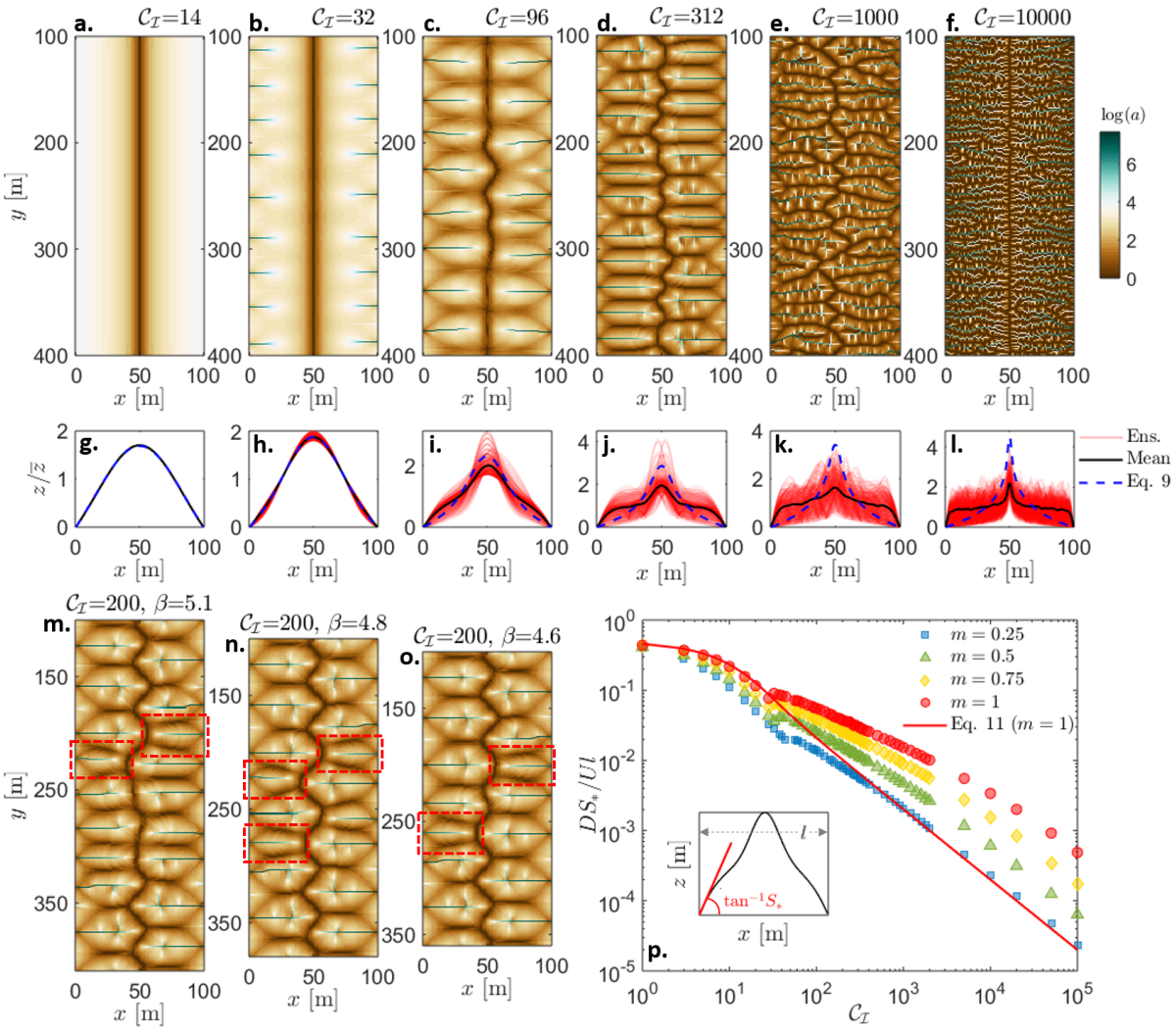

Fig. 5. Rectangular domains. Ridge/valley networks obtained for $m = n = 1$ over rectangular domains with (a-f) $\beta = 5$ ($\mathcal{C}_I$ = 14, 32, 96, 312, 1000, and 10000), (m) $\beta = 5.1$ ($\mathcal{C}_I$ = 200), (n) $\beta = 4.8$ ($\mathcal{C}_I$ = 200), and (o) $\beta = 4.6$ ($\mathcal{C}_I$ = 200). β is a shape factor defined as the ratio between the two horizontal length scales l_y and l_x, namely $\beta = l_y/l_x$. Examples of dislocation defects are shown by the red dashed rectangles in panels m-o. (g-l) Normalized elevation profiles along the x axis for the six simulations of panels a-f: black lines are the mean elevation profiles, red lines show the ensemble of all the profiles along x, blue dashed lines are analytical elevation profiles for the unchannelized case – Eq. (9). Mean elevation profiles along the x axis were computed as average values of the elevation profiles neglecting the extremal parts (100 m length) of the domain. (p) Slope of the mean elevation profile S_* as a function of $\mathcal{C}_I$ for simulations with $n = 1$ and m = 0.25, 0.5, 0.75, and 1. The solid red line represents the analytical solution for $m = 1$ (Eq. (11)) for the unchannelized case. The schematic in the inset shows the definition of S_* and l used in the vertical axis of the chart.

branching (54) and thus on the dominant erosional mechanisms acting on the landscape (i.e., interplay between runoff erosion, soil creep, and uplift) and the various landscape properties affecting diffusion and erosion coefficients, such as soil type, vegetation cover, and climate. When diffusion dominates, hypsometric curves display a less pronounced basal convexity (54). A systematic analysis of real topographies in terms of statistics of hypsometry, branching angles, and characteristic spacing would help infer values of $\mathcal{C}_I$ and the non-linearity exponents m and n of natural landscapes, and possibly link them to the abiotic and biotic properties of the landscape under consideration.

It will also be interesting to explore the differences in transient dynamics between the hypsometry of juvenile and old landscapes. It is likely that, during the early stages of the basin development when the drainage network is formed, the hypsometric curve presents a more pronounced basal convexity (2) regardless of the value of $\mathcal{C}_I$, progressively transitioning toward its quasi-equilibrium form during the "relaxation phase" (55). Such slow relaxations (e.g., Fig. 5), often towards slightly irregular configurations rather than perfectly regular networks, are reminiscent of the presence of defects in crystals and the amorphous configurations originating in glass transition (56).

Materials and Methods

Analytical solutions for $m = n = 1$. To derive one-dimensional steady state solutions of the coupled PDE system (Eqs. (4)-(5)) we consider a symmetric hillslope of length l in the x-direction, with divide at $x = 0$ (see inset in Fig. 4a). Assuming a fixed elevation $z = 0$ at $x = \pm l/2$, the steady steady solution of the coupled system

of Eqs. (4) and (5) for $m = n = 1$ reads (44)

$$a_0 = |x| \quad [8]$$

$$z_0 = \frac{U}{2D}\left[\left(\frac{l}{2}\right)^2 \mathcal{H}\left(1,1;\frac{3}{2},2;-\frac{K_a\left(\frac{l}{2}\right)^2}{D}\right) - x^2\mathcal{H}\left(1,1,;\frac{3}{2},2;-\frac{K_a x^2}{D}\right)\right] \quad [9]$$

where subscript 0 denotes the basic steady state, and $\mathcal{H}(.,.;.,.;.)$ is the generalized hypergeometric function (57). In these conditions, the local slope $S_0 = dz_0/dx$ can also be derived analytically as (44)

$$S_0 = \frac{\sqrt{2}U\mathcal{D}\left(\frac{\sqrt{K_a}x}{\sqrt{2D}}\right)}{\sqrt{DK_a}} \quad [10]$$

where $\mathcal{D}(.)$ is the Dawson's integral (57).

Linear stability analysis. We studied the stability of the basic state (Eqs. (8)-(9)) to perturbations $\tilde{a}$ and $\tilde{z}$ in the y-direction. Boundary conditions are zero sediment and specific drainage area at the hilltop ($\tilde{a} = d\tilde{z}/dx = 0$ at $x = 0$) and fixed elevation at the domain boundary ($\tilde{z} = 0$ at $x = l/2$). We use normal mode analysis and write perturbations in the classical form $\tilde{a} = \phi(x)e^{iky+\sigma t}$ and $\tilde{z} = \psi(x)e^{iky+\sigma t}$ (plus complex conjugate), where k and σ are the wavenumber and the growth rate of the perturbations, respectively. The perturbed system can be re-cast in terms of a third order non-constant coefficient differential eigenvalue problem of the form $\gamma_1(x)\phi'''(x) + \gamma_2(x)\phi''(x) + \gamma_3(x)\phi'(x) + \gamma_4(x)\phi(x) = \sigma\gamma_5(x)\phi'(x)$. Solutions to the stability problem are obtained by means of a spectral Galerkin technique with numerical quadrature (58, 59). Among the discrete set of eigenvalues obtained, we tracked the behavior of the least stable (i.e., with largest real part). The stability analysis was performed here for unitary exponents m and n due to the availability of an analytical form of the basic state. Numerical results for a wider range of m and n values are reported in the SI Appendix (Fig. S9).

Numerical simulations. Numerical simulations were performed using forward differences in time and centered difference approximations for the spatial derivatives, considering regular square grids of lateral dimension l, as well as on rectangular domains with shape factor β, defined as the ratio between the domain dimensions in the y and x direction (i.e., $\beta = l_y/l_x$). Specifically, in the simulations over rectangular domains we fixed the length in the x direction (i.e., $l_x = 100$ m), and varied only the length l_y in the y direction. The total drainage area A was computed at each grid point with the $D\infty$ algorithm, while a was then approximated as $A/\Delta x$ (43, 60), with Δx the grid size. Simulations were run assuming $\Delta x = 1$ m (additional numerical experiments, shown in the SI Appendix (Fig. S1), were performed for different grid sizes to validate the independence of the resulting patterns on the grid resolution). Convex profiles were used as initial condition. Over wide rectangular domains for $\mathcal{C}_\mathcal{I} \geq 320$ a white noise with standard deviation equal to 10^{-6} m was also added in the initial condition. A sensitivity analysis was conducted over square domains (not shown) to make sure that the resulting spatial organization of ridges and valleys at steady state was robust to the choice of initial conditions. We considered a wide range of $\mathcal{C}_\mathcal{I}$ values (from 10^0 to 10^5) constructed by using literature values of the system parameters, which are generally estimated in terms of time-averaged values from experimental hillslope shapes (61) or high resolution topographies (18, 19).

Dimensional analysis of the channelization transition. We proceed similarly to the analysis of turbulence transition in pipes and channels. There the relationship between the friction factor ξ and the Reynolds number Re can be obtained by first relating the wall shear stress $\tau = \mu d\overline{u}/dx^*|_{x^*=0}$, where $\overline{u}$ is the streamwise mean velocity profile and x^* is the distance from the wall, to its governing quantities as $\tau = \Xi(V, L, \mu, \rho, \epsilon)$, where ρ is the density, μ the viscosity, V the mean velocity, L the characteristic lateral dimension, and ϵ the roughness height. The Pi-Theorem then may be used to express the head loss per unit length (g is gravitational acceleration) as $S_h = \frac{4\tau}{g\rho L} = \frac{V^2}{2gL}\xi\left(Re, \frac{\epsilon}{L}\right)$, see ref. 62. Analogously, here we can relate the slope of the mean elevation profile at the hillslope base $S_* = d\overline{z}/dx|_{x=l/2}$ to the parameters and characteristics of the landscape evolution model as $S_* = \Phi(D, K_a, m, U, l)$ (we consider here $n = 1$). Choosing l, U, and D as dimensionally independent variables, the Pi-Theorem yields $DS_*/Ul = \varphi(\mathcal{C}_\mathcal{I}, m)$, where the quantity DS_* quantifies the diffusive outgoing sediment flux per unit width (along the x-axis) at the boundary, while the term Ul represents the incoming sediment flux by tectonic uplift per unit width. Such a functional relationship can be analytically derived for the unchannelized case when $m = 1$ from Eq. (10) as

$$\frac{DS_*}{Ul} = \left(\frac{\mathcal{C}_\mathcal{I}}{2}\right)^{-1/2}\mathcal{D}\left[\left(\frac{\mathcal{C}_\mathcal{I}}{8}\right)^{1/2}\right]. \quad [11]$$

In the numerical simulations, S_* was computed as the slope of the linear fit to the mean elevation profile in the first 3 meters at the hillslope base (see inset in Fig. 5p).

Data and code availability. 1-meter resultion LiDAR data for Calhoun and Gabilan Mesa can be dowloaded from the OpenTopography facility (https://opentopography.org). The code used for the numerical simulations is described in ref. 63 and available on GitHub (https://github.com/ShashankAnand1996/LEM).

ACKNOWLEDGMENTS. We acknowledge support from the US National Science Foundation (NSF) grants EAR-1331846 and EAR-1338694, and BP through the Carbon Mitigation Initiative (CMI) at Princeton University.The useful comments of the anonymous reviewers are also gratefully acknowledged. LiDAR data for Calhoun and Gabilan Mesa were obtained from the National Center for Airborne Laser Mapping (NCALM) with support from the US National Science Foundation (EAR-1339015, EAR-1331846, EAR-1043051) and retrieved from https://opentopography.org.

1. R E Horton. Erosional development of streams and their drainage basins; hydrophysical approach to quantitative morphology. *Geological Society of America Bulletin*, 56(3):275–370, 1945.
2. A N Strahler. Hypsometric (area-altitude) analysis of erosional topography. *Geological Society of America Bulletin*, 63(11):1117–1142, 1952.
3. R L Shreve. Statistical law of stream numbers. *The Journal of Geology*, 74(1):17–37, 1966.
4. T R Smith and F P Bretherton. Stability and the conservation of mass in drainage basin evolution. *Water Resources Research*, 8:1506–1529, 1972.
5. D S Loewenherz. Stability and the initiation of channelized surface drainage: a reassessment of the short wavelength limit. *Journal of Geophysical Research: Solid Earth*, 96(B5):8453–8464, 1991.
6. N Izumi and G Parker. Inception of channelization and drainage basin formation: upstream-driven theory. *Journal of Fluid Mechanics*, 283:341–363, 1995.
7. D G Tarboton, R L Bras, and I Rodriguez-Iturbe. The fractal nature of river networks. *Water Resources Research*, 24(8):1317–1322, 1988.
8. A Marani, R Rigon, and A Rinaldo. A note on fractal channel networks. *Water Resources Research*, 27(12):3041–3049, 1991.
9. I Rodríguez-Iturbe and A Rinaldo. *Fractal river basins: chance and self-organization*. Cambridge University Press, 2001.
10. P S Dodds and D H Rothman. Scaling, universality, and geomorphology. *Annual Review of Earth and Planetary Sciences*, 28(1):571–610, 2000.
11. R Rigon, A Rinaldo, I Rodriguez-Iturbe, R L Bras, and E Ijjasz-Vasquez. Optimal channel networks: a framework for the study of river basin morphology. *Water Resources Research*, 29(6):1635–1646, 1993.
12. J R Banavar, F Colaiori, A Flammini, A Giacometti, A Maritan, and A Rinaldo. Sculpting of a fractal river basin. *Physical Review Letters*, 78(23):4522, 1997.
13. E Somfai and L M Sander. Scaling and river networks: A Landau theory for erosion. *Physical Review E*, 56(1):R5, 1997.
14. R Pastor-Satorras and D H Rothman. Scaling of a slope: the erosion of tilted landscapes. *Journal of Statistical Physics*, 93(3-4):477–500, 1998.
15. S Kramer and M Marder. Evolution of river networks. *Phys. Rev. Lett.*, 68:205–208, 1992.
16. A Arneodo, F Argoul, E Bacry, J F Muzy, and M Tabard. Golden mean arithmetic in the fractal branching of diffusion-limited aggregates. *Physical review letters*, 68(23):3456, 1992.
17. A Fowler. *Mathematical geoscience*. Springer Science & Business Media, 2011.
18. J T Perron, W E Dietrich, and J W Kirchner. Control on the spacing of first-order valleys. *Journal of Geophysical Research*, 113:F04016, 2008.
19. J T Perron, P W Richardson, K L Ferrier, and M Lapôtre. The root of branching river networks. *Nature*, 492(7427):100, 2012.
20. J C Gallant and M F Hutchinson. A differential equation for specific catchment area. *Water Resources Research*, 47(5), 2011.
21. S Bonetti, A D Bragg, and A Porporato. On the theory of drainage area for regular and non-regular points. *Proc. R. Soc. A*, 474(2211):20170693, 2018.
22. S B Pope. *Turbulent Flows*. Cambridge University Press, Cambridge, UK, 2000.
23. P G Drazin and W H Reid. *Hydrodynamic Stability*. Cambridge Mathematical Library. Cambridge University Press, 2 edition, 2004. .
24. P K Kundu, I M Cohen, and D W Dowling. *Fluid Mechanics 5th ed.* Elsevier, 2011.

25. A Rinaldo, A Maritan, F Colaiori, A Flammini, R Rigon, I Rodriguez-Iturbe, and J R Banavar. Thermodynamics of fractal networks. *Physical Review Letters*, 76(18):3364, 1996.
26. H Ozawa, A Ohmura, R D Lorenz, and T Pujol. The second law of thermodynamics and the global climate system: A review of the maximum entropy production principle. *Reviews of Geophysics*, 41(4), 2003.
27. L M Martyushev and V D Seleznev. Maximum entropy production principle in physics, chemistry and biology. *Physics reports*, 426(1):1–45, 2006.
28. D Bensimon, L P Kadanoff, S Liang, B I Shraiman, and C Tang. Viscous flows in two dimensions. *Reviews of Modern Physics*, 58(4):977, 1986.
29. L M Sander and E Somfai. Random walks, diffusion limited aggregation in a wedge, and average conformal maps. *Chaos: An Interdisciplinary Journal of Nonlinear Science*, 15(2): 026109, 2005.
30. M R Errera and A Bejan. Deterministic tree networks for river drainage basins. *Fractals*, 6 (03):245–261, 1998.
31. S Lorente, W Wechsatol, and A Bejan. Tree-shaped flow structures designed by minimizing path lengths. *International Journal of Heat and Mass Transfer*, 45(16):3299–3312, 2002.
32. A Bejan. *Advanced engineering thermodynamics*. John Wiley & Sons, 2016.
33. O Devauchelle, A P Petroff, H F Seybold, and D H Rothman. Ramification of stream networks. *Proceedings of the National Academy of Sciences*, 109(51):20832–20836, 2012.
34. R Yi, Y Cohen, H Seybold, E Stansifer, R McDonald, M Mineev-Weinstein, and D H Rothman. A free-boundary model of diffusive valley growth: theory and observation. *Proc. R. Soc. A*, 473(2202):20170159, 2017.
35. W E Dietrich, D G Bellugi, L S Sklar, J D Stock, A M Heimsath, and J J Roering. Geomorphic transport laws for predicting landscape form and dynamics. *Prediction in Geomorphology*, pages 103–132, 2003.
36. T R Smith. A theory for the emergence of channelized drainage. *Journal of Geophysical Research: Earth Surface*, 115(F2), 2010.
37. W E H Culling. Analytical theory of erosion. *The Journal of Geology*, 68(3):336–344, 1960.
38. W E H Culling. Soil creep and the development of hillside slopes. *The Journal of Geology*, 71(2):127–161, 1963.
39. A D Howard. A detachment-limited model of drainage basin evolution. *Water Resources Research*, 30(7):2261–2285, 1994.
40. I Rodríguez-Iturbe, A Rinaldo, R Rigon, R L Bras, A Marani, and E Ijjász-Vásquez. Energy dissipation, runoff production, and the three-dimensional structure of river basins. *Water Resources Research*, 28(4):1095–1103, 1992.
41. J D Pelletier. Fluvial and slope-wash erosion of soil-mantled landscapes: detachment-or transport-limited? *Earth Surface Processes and Landforms*, 37(1):37–51, 2012.
42. A Chen, J Darbon, and J-M Morel. Landscape evolution models: A review of their fundamental equations. *Geomorphology*, 219:68–86, 2014.
43. D G Tarboton. A new method for the determination of flow directions and upslope areas in grid digital elevation models. *Water Resources Research*, 33(2):309–319, 1997.
44. S Bonetti, D D Richter, and A Porporato. The effect of accelerated soil erosion on hillslope morphology. *Earth Surface Processes and Landforms*, 2019.
45. A Bejan and S Lorente. Design with constructal theory. 2008.
46. B B Mandelbrot. *The fractal geometry of nature*, volume 1. WH freeman New York, 1982.
47. I Rodriguez-Iturbe, A Rinaldo, R Rigon, R L Bras, E Ijjasz-Vasquez, and A Marani. Fractal structures as least energy patterns: The case of river networks. *Geophysical Research Letters*, 19(9):889–892, 1992.
48. A Flammini and F Colaiori. Exact analysis of the Peano basin. *Journal of Physics A: Mathematical and General*, 29(21):6701, 1996.
49. D R Montgomery, G Balco, and S D Willett. Climate, tectonics, and the morphology of the Andes. *Geology*, 29(7):579–582, 2001.
50. L E L Lowman and A P Barros. Investigating links between climate and orography in the central Andes: Coupling erosion and precipitation using a physical-statistical model. *Journal of Geophysical Research: Earth Surface*, 119(6):1322–1353, 2014.
51. J T Perron, J W Kirchner, and W E Dietrich. Formation of evenly spaced ridges and valleys. *Nature*, 460:502–505, 2009.
52. M C Cross and P C Hohenberg. Pattern formation outside of equilibrium. *Reviews of Modern Physics*, 65(3):851, 1993.
53. R L Panton. *Incompressible Flow. Third Edition*. John Wiley & Sons, 1984.
54. G Willgoose and G Hancock. Revisiting the hypsometric curve as an indicator of form and process in transport-limited catchment. *Earth Surface Processes and Landforms*, 23(7):611–623, 1998.
55. S Bonetti and A Porporato. On the dynamic smoothing of mountains. *Geophysical Research Letters*, 44(11):5531–5539, 2017.
56. P G Debenedetti and F H Stillinger. Supercooled liquids and the glass transition. *Nature*, 410 (6825):259, 2001.
57. M Abramowitz and I A Stegun. *Handbook of mathematical functions*. Dover, New York, 1964.
58. C G Canuto, M Y Hussaini, A Quarteroni, and T A Zang. *Spectral methods: Fundamentals in single domains*. Springer, Berlin, 2006.
59. C Camporeale, C Canuto, and L Ridolfi. A spectral approach for the stability analysis of turbulent open-channel flows over granular beds. *Theoretical and Computational Fluid Dynamics*, 26(1-4):51–80, 2012.
60. Giovanni Battista Chirico, Andrew W Western, Rodger B Grayson, and Günter Blöschl. On the definition of the flow width for calculating specific catchment area patterns from gridded elevation data. *Hydrological Processes: An International Journal*, 19(13):2539–2556, 2005.
61. K E Sweeney, J J Roering, and C Ellis. Experimental evidence for hillslope control of landscape scale. *Science*, 349(6243):51–53, 2015.
62. B R Munson, D F Young, T H Okiishi, and W W Huebsch. *Fundamentals of fluid mechanics*. John Wiley & Sons, 1995.
63. S. K. Anand, M. Hooshyar, and A. Porporato. Linear layout of multiple flow-direction networks for landscape-evolution simulations. *arXiv preprint arXiv:1909.03176*, 2019.